Exploring synchrony and chaos of parahydrogen-pumped two-compartment radio-frequency amplification by stimulated emission of radiation

Lars Lohmann [1,*,†] Sören Lehmkuhl [2,*,‡] Simon Fleischer [1,2] Matthew S. Rosen [3,4] Eduard Y. Chekmenev [5,6]
Thomas Theis [7,8,9] Alina Adams [1] and Stephan Appelt [1,10,§]

[1]*Institute of Technical and Macromolecular Chemistry, RWTH Aachen University, 52056 Aachen, Germany*
[2]*Institute of Microstructure Technology, Karlsruhe Institute of Technology, 76344 Eggenstein-Leopoldshafen, Germany*
[3]*Massachusetts General Hospital, A. A. Martinos Center for Biomedical Imaging, Boston, Massachusetts 02129, USA*
[4]*Department of Physics, Harvard University; Cambridge, Massachusetts 02138, USA*
[5]*Department of Chemistry, Integrative Biosciences (IBio), Karmanos Cancer Institute (KCI),*
Wayne State University Detroit, Michigan 48202, USA
[6]*Russian Academy of Sciences, Leninskiy Prospekt 14, Moscow 119991, Russia*
[7]*Department of Chemistry, North Carolina State University, Raleigh, North Carolina 27606, USA*
[8]*Department of Physics, North Carolina State University, Raleigh, North Carolina 27695, USA*
[9]*Joint Department of Biomedical Engineering, University of North Carolina at Chapel Hill and North Carolina State University,*
Raleigh, North Carolina 27695, USA
[10]*Central Institute for Engineering, Electronics and Analytics–Electronic Systems (ZEA-2),*
Forschungszentrum Jülich GmbH, D-52425 Jülich, Germany

A nuclear-spin-based RASER (radio-frequency amplification by stimulated emission of radiation) is an ideal experimental system to explore nonlinear interaction phenomena of nuclear spins coupled via virtual photons to a resonator. This is due to the RASER being stable for several hours, allowing for extended observation of these phenomena. Nonlinear phenomena in multimode RASERs range from mode oscillations in synchrony, frequency shifts, frequency combs, period doublings, and even chaos. These phenomena are observed in a parahydrogen-pumped two-compartment proton RASER. In two independently pumped compartments, the separation in frequency space between the two RASER modes is precisely controlled with a magnetic field gradient. By controlling the mode separation, we can select the type of nonlinear phenomena observed. A key finding is that the ranges of mode separation where chaos and synchrony occur are very close together. The experimental results are supported by numerical simulations, based on two-mode RASER equations.

I. INTRODUCTION

RASER (radio-frequency amplification by stimulated emission of radiation) emission in nuclear spin 1/2 systems requires a population inversion between two Zeeman levels, $d_0 = N_2 - N_1$. This population inversion can be generated via hyperpolarization techniques, where a large negative nuclear spin polarization can be created, corresponding to a positive population inversion d_0.

The most common hyperpolarization techniques include dynamic nuclear polarization (DNP) [1–4], spin exchange optical pumping (SEOP) [5–8], metastability exchange optical pumping (MEOP) [9], and parahydrogen (p-H_2)-based approaches such as para-hydrogen-induced polarization (PHIP) [10–14] and signal amplification by reversible exchange (SABRE) [15–19]. These hyperpolarization schemes have been used to establish nuclear spin based RASERs operating in the gas [20–22], liquid [23–26], and solid phase [27–30].

SABRE is an efficient way to continuously hyperpolarize (or pump) a liquid state ^1H RASER at room temperature and at low and high magnetic field [15,31]. In SABRE, p-H_2 and target substrates reversibly coordinate to a metal-organic catalyst with a system-specific contact time. During this time, the singlet state of p-H_2 is transferred and converted via J couplings into a highly polarized state of the target nuclei [15,16]. Using this approach, the first para-hydrogen-pumped ^1H RASER demonstrated a substantial increase in the precision of J-coupled nuclear magnetic resonance (NMR) spectroscopy [32]. Subsequent work on SABRE- and PHIP-pumped ^1H RASERs at high and low magnetic fields have shown strong connections to nonlinear science and have extended the range of possible applications. These include high-resolution NMR spectroscopy, gyroscopes and magnetometry, membrane-pumped RASERs, RASER-induced multinuclear signal enhancement, and RASER MRI [31,33–39].

---

*These authors contributed equally to this work.

†Corresponding author: lars.lohmann@rwth-aachen.de

‡Corresponding author: soeren.lehmkuhl@kit.edu

§Corresponding author: st.appelt@fz-juelich.de

In the present work, we analyze nonlinear phenomena in these systems including synchrony and chaos. These two are fundamental phenomena which play an essential role in many disciplines of science and technology [40–44]. In the context of a two-mode RASER, synchrony means that both modes oscillate at a single frequency with a fixed phase relationship between them [44]. This results in a single line in the RASER spectrum. For a two-mode RASER, chaotic motion is associated with a continuum of spectral lines, and the temporal characteristics of the RASER signal are very sensitive to the initial conditions [35,44].

Chaos arises in many nonlinearly interacting systems, including nuclear spin 1/2 systems. [23,45–47] Recently, ^{1}H RASER experiments have shown that chaos and intermittence can occur in a p-H_2-pumped NMR RASER at 1.45 tesla [35]. However, for these experiments, the population inversion d_0 was generated outside of the magnet through a hydrogenation reaction of vinyl acetate and hydroxyethyl propionate. This initial population inversion was very high at $d_0 \sim 10^{19}$, and consequently the system "passed" through several nonlinear regimes while d_0 was decaying over time. Spectra corresponding to two RASER modes of J-coupled lines were observed for about 1 min. Period doubling and chaos were also observed over short time windows (≈ 2 s). This motivates the precise study of nonlinear phenomena in RASER systems. Limitations of previous work include the transient (non-steady-state) nature of the acquired signals as well as the fixed frequency difference between the modes given by the J coupling [35].

Here we describe an experimental system designed for precise measurements of chaos, multiple-period doubling, and synchrony in RASER systems. Stable continuous RASER emission is generated using SABRE pumping and proton inductive detection at 7.8 mT at a proton resonance frequency of 333.3 kHz. Under these conditions, crucial experimental parameters for RASER emission remain constant [33,39], as will be discussed in Secs. II and III. A frequency separation between two RASER modes is achieved and controlled by a magnetic field gradient G_z over two individually pumped compartments. Both compartments are pumped independently by a continuous parahydrogen (p-H_2) gas flow, generating two stable ^{1}H RASER modes which oscillate at two distinct frequencies. The separation between the two modes can be adjusted to arbitrary values by controlling the strength of a magnetic field gradient G_z. Here the nonlinear phenomena are dominated by radiation damping. Distant dipolar field effects are averaged out through motion induced by the p-H_2 flow and primarily lead to an equal frequency shift of both modes (see Appendix D). The resulting stable continuous RASER signals can be observed over periods of minutes and allow for a precise Fourier analysis of the signal to identify all mentioned nonlinear phenomena.

II. EXPERIMENTAL

The experimental realization of the SABRE-pumped two-compartment RASER is illustrated in Fig. 1. All experiments were conducted in an electromagnet with a static magnetic B_0 field ranging from 0 to 20 mT. Four shimming coils (G_x, G_y, G_z, and G_z^2) were used to attain a magnetic field homogeneity
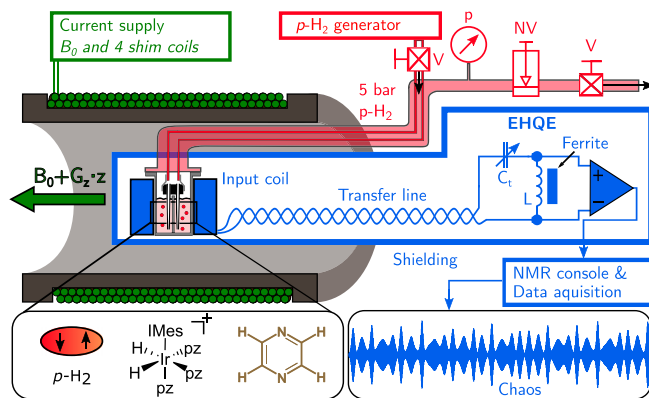

FIG. 1. Experimental setup of the SABRE-pumped two-compartment ^{1}H RASER, adapted from Suefke *et al.* [32], depicting the parahydrogen (p-H_2) supply (red) consisting of the generator, valves (V), a needle valve (NV), pressure gauge (p), and the injection capillaries, as well as the external high-quality enhanced (EHQE) NMR circuit[48] (blue) and the magnetic field B_0 with gradient-induced additional term z G_z (green). Bottom left: para-hydrogen molecule (p-H_2) together with SABRE catalyst IMes-Ir used to create negative polarization $P_H \approx -3 \times 10^{-3}$ of pyrazine (pz). Bottom right: Example for a ^{1}H chaotic signal of pyrazine measured over a time period of 20 s.

of about 1 ppm over a volume of $0.5\,\text{cm}^3$. The gradient strength $G_z = C_z I_z$ [constant $C_z = 0.192\,\text{mG}/(\text{cm} \times \text{mA})$] was varied throughout the experiments by changing the current I_z. For sensitive NMR detection, a cylindrical coil (inner diameter = 10 mm, height = 10 mm) was connected to an external ferrite LC-resonator with a quality factor of $Q_{ext} \approx 300$. The combined input coil with external resonator had a total $Q \approx 100$ (EHQE-NMR [48]) at a ^{1}H detection frequency of 333.3 kHz ($B_0 = 7.8$ mT). The ^{1}H RASER signal was fed into a low-noise preamplifier and a custom-made lock-in amplifier. Typical signal acquisition times were 100 s with a data acquisition rate of a few kHz. In these RASER experiments, off-resonance frequencies varied between 40 and 160 Hz.

The liquid sample was contained in a cylindrical dual-chamber glass sample cell (inner radius $r = 4$ mm) with a volume of $0.21\,\text{cm}^3$ per chamber. The two chambers were separated by a glass slide with $s = 1$ mm thickness (see Fig. 3). The total sample volume was $V_s = 0.42\,\text{cm}^3$, and the sensitive volume of the detection coil was $\approx 0.64\,\text{cm}^3$, resulting in a filling factor (the fraction of the coil detection volume filled with sample) estimated as $\eta = 0.66$.

The required p-H_2 delivery was realized by a custom-made glass setup (see Fig. 1) in combination with one glass capillary injecting gas into each chamber filled with the SABRE solution (~ 100 μm outer capillary diameter, ~ 30 μm inner diameter). The p-H_2 flow rate and pressure were controlled with a needle valve in combination with a flow meter and a pressure gauge. The p-H_2 gas pressure was varied between 2 and 7 bar with nearly equal p-H_2 flow rate in both chambers ranging from 10 to 100 sccm (standard cubic centimeters per minute). The H_2 gas (grade 5; purity >99.999%) was enriched to 92%−93% p-H_2 using a Bruker BPHG 90 p-H_2 generator. The sample solution was based on
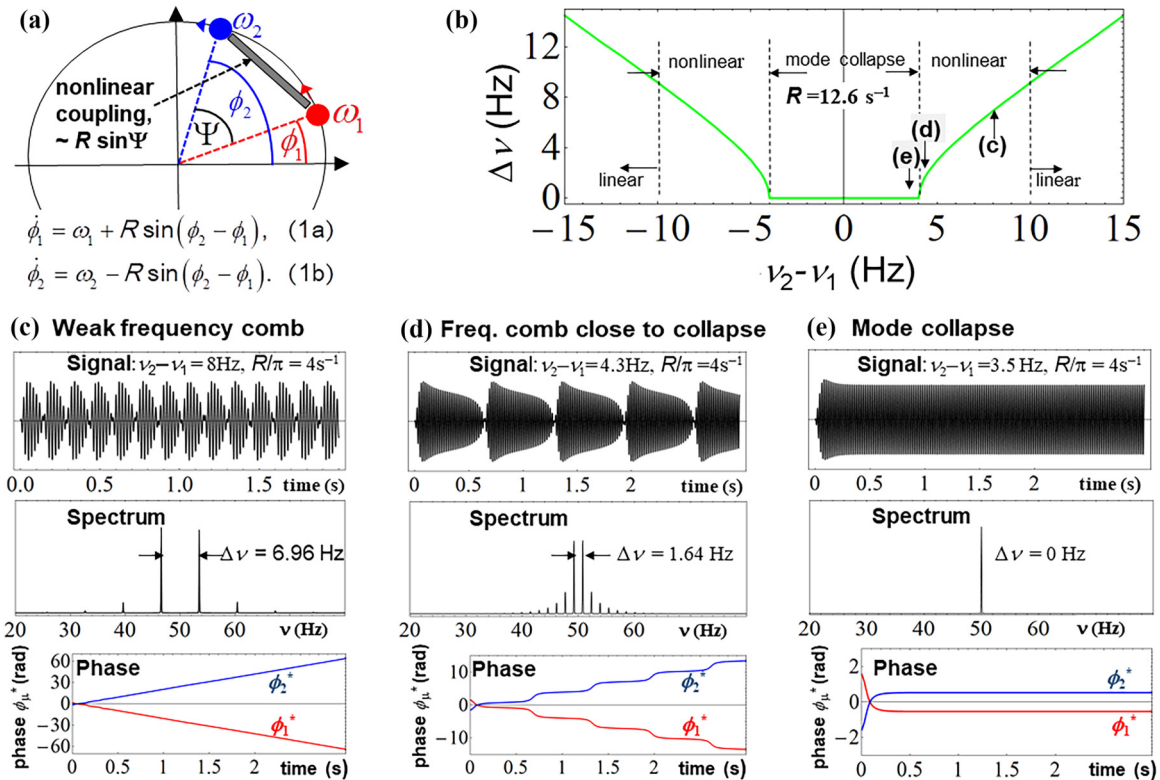
FIG. 2. Fourier and phase analysis of two nonlinear coupled oscillators. (a) Two beads at angular positions ϕ_2 and ϕ_1 rotate with angular frequencies ω_2 and ω_1. (b) Numerical evaluation of separation $\Delta\nu$ vs $\nu_2 - \nu_1$ based on Eqs. (1a) and (1b) and $R = 12.6\,\mathrm{s}^{-1}$. Dotted lines separate the linear, nonlinear, and mode-collapse regimes, where the vertical arrows indicate the three cases (c)–(e), with $\nu_2 - \nu_1 = 8\,\mathrm{Hz}$ (c), $\nu_2 - \nu_1 = 4.3\,\mathrm{Hz}$ (d), and $\nu_2 - \nu_1 = 3.5\,\mathrm{Hz}$ (e), respectively. Three top panels in (c)–(e) indicate simulated signals $S = \cos\phi_1 + \cos\phi_2$, with their corresponding spectra (middle), and the phase evolution $\phi_\mu^* = \phi_\mu - 2\pi\nu_0 t$, $\mu = 1, 2$ (bottom). The spectra (middle) with a center frequency of $\nu_0 = 50\,\mathrm{Hz}$ are transformed in the absolute mode over the time slice [100 s, 200 s] using a Gauss filter. The three panels in the bottom show different phase evolutions starting with the same initial conditions $\phi_2(0) = -\pi/2$ and $\phi_1(0) = \pi/2$.

a composition known to yield high proton hyperpolarization using SABRE [15,17] and prepared and handled under inert gas conditions. A methanol-d_4 solution contained the catalyst precursor ([IrCl(COD)(IMes)]) at 5 mmol/L as well as the target molecule pyrazine at $c_{\mathrm{pyr}} = 100\,\mathrm{mmol/L}$ [49].

Pyrazine was chosen as the target molecule because it only has a single-proton NMR resonance with $n_{\mathrm{pyr}} = 4$ chemically and magnetically equivalent protons. The catalyst was activated *in situ* with a continuous p-H_2 flow of 40–70 sccm at 4 to 5 bar overpressure for several minutes prior to each experiment. p-H_2 overpressure also helps minimizing solvent evaporation, although the p-H_2 bubbling does cause methanol-d_4 loss over time, limiting the measurement times to about 1.5 h at a p-H_2 flow rate of 70 sccm. The build-up of population inversion d_0 during the activation was monitored by applying multiple 90° excitation pulses until the RASER threshold is reached, which is marked by continuous RASER oscillations. The pumping rate Γ of the SABRE process was measured during the initial startup of the RASER signal. Typical values for Γ in the SABRE experiments were between 0.08 and 0.16 s^{-1}. At flow rates <70 sccm, the polarization is not high enough to observe period doubling or chaos. T_1, T_2^* for the pyrazine sample were measured, ranging from 5 to 12 s and from 0.4 to 0.7 s, respectively, depending on the actual concentration of pyrazine and catalyst which both change slowly over time due to methanol evaporation.

Each chamber generates its own mode in the presence of a gradient, which is elaborated in detail in Sec. III. To generate a mode separation $\Delta\nu = \nu_2 - \nu_1$, the current I_z was varied in the range from -20 to $+16\,\mathrm{mA}$. For the given C_z, this corresponds to a range of gradients $-3.84\,\mathrm{mG/cm} < G_z < 3.07\,\mathrm{mG/cm}$. Continuous RASER signals at different mode separations were acquired for 50–100 s at each given gradient $G_z = C_z I_z$.

III. THEORETICAL MODEL

A two-mode RASER model based on the RASER theory [33,35] and with the additional inclusion of a magnetic field gradient is described here to analyze and understand the experimental results. In Sec. II A, a frequency and phase analysis is presented for two nonlinearly coupled oscillators moving in the one-dimensional angular Ψ space (1D model). Next, in Sec. II B, the gradient-controlled two-compartment RASER equations moving in the three-dimensional (d, A, Ψ) space are presented (3D model). An intermediate case in the (A, Ψ) space (2D model) is derived in Appendix B. All three models are compared in Sec. IV.

A. Two nonlinear coupled oscillators in 1D Ψ space

In this subsection we present a Fourier and phase analysis of two nonlinear coupled oscillators in one dimension. The

model is used to explain several phenomena, such as nonlinear frequency shifts, frequency comb, and synchronous motion (i.e., spectral line collapse). Furthermore, the results are used as a reference to compare with the exact two-compartment RASER model (Sec. III B). The model is represented by two rotating beads [Fig. 2(a)] at angular positions ϕ_1 and ϕ_2, which oscillate with angular frequencies ω_1 and ω_2. The two oscillators are assumed to be frictionless and are coupled by a nonlinear element described by $R\cos(\phi_2 - \phi_1)$, where R is the strength of the coupling in units (s^{-1}). The governing equations of motion [44] are given in the bottom of Fig. 2(a). Here we focus on a Fourier and phase analysis of the two nonlinearly coupled oscillators and on the expected dependence of the predicted mode separation $\Delta\nu$ as a function of the frequency difference $\nu_2 - \nu_1$. It is convenient to introduce the phase difference $\Psi = \phi_2 - \phi_1$, which represents the angular variable of motion in one dimension. The equation of motion with respect to Ψ is obtained by subtraction of the two equations in the bottom of Fig. 2(a), which results in

$$\dot{\Psi} = (\omega_2 - \omega_1) - 2R\sin\Psi. \tag{1}$$

Figures 2(c)–2(e) show the numerical evaluation of the projected total signal amplitudes $\cos\phi_2(t) + \cos\phi_1(t)$ (top), with the corresponding Fourier transformed spectrum (middle trace) and the evolution of the two transformed phases $\phi_2^*(t)$ and $\phi_1^*(t)$ (bottom). The star indicates the transformation of the phases ϕ_2 and ϕ_1 into a frame which rotates with the angular frequency $\omega_0 = (\omega_2 + \omega_1)/2$, which means explicitly $\phi_2^* = \phi_2 - \omega_0 t$ and $\phi_1^* = \phi_1 - \omega_0 t$. In the first case in Fig. 2(c), where $|\omega_2 - \omega_1| > 2R$ ($|\nu_2 - \nu_1| > R/\pi$) holds, the two modes oscillate nearly independently, and the corresponding spectrum (middle) is characterized by two lines at frequencies ν_2 and ν_1 centered at $\nu_0 = 0.5(\nu_2 + \nu_1)$ and separated by $\Delta\nu \approx \nu_2 - \nu_1$. The two lines are accompanied on both sides by smaller lines, and two consecutive lines are all separated by $\Delta\nu$. The transformed phases (bottom) evolve as a linear function of time, $\phi_2^* = (\omega_2 - \omega_0)t$ and $\phi_1^* = (\omega_1 - \omega_0)t$, so $d/dt(\phi_2^* - \phi_1^*) = (\omega_2 - \omega_1)$. Provided that $|\nu_2 - \nu_1| \gg R/\pi$, all side lines of the frequency comb vanish, and the spectrum is characterized by exactly two lines at frequencies ν_2 and ν_1 and separated by $\Delta\nu = \nu_2 - \nu_1$. In the second case in Fig. 2(d), close to $|\omega_2 - \omega_1| \approx 2R$ and $|\omega_2 - \omega_1| > 2R$, the spectrum is a dense frequency comb with several side lines and with a center frequency at ν_0. The separation between two consecutive lines is $\Delta\nu \ll |\nu_2 - \nu_1|$. The two phases ϕ_2^* and ϕ_1^* are linear functions of time on average, and the slope is smaller than $|\omega_{1,2} - \omega_0|$. Each phase is superimposed by periodic wiggles which reflect phase modulations caused by the nonlinear interaction. The observed frequency comb in the spectrum is a result of this phase modulation. In the third case in Fig. 2(e), $|\omega_2 - \omega_1| < 2R$, the signal (top) oscillates like a pure cosine, and the corresponding spectrum has collapsed into one line at the center frequency ν_0. After a short transient evolution of about 100 ms (see bottom) the two phases become constant but not equal. The two modes oscillate in synchrony at one frequency ν_0 with a fixed phase difference, $\Psi_s = (\phi_2^* - \phi_1^*)_s = \arcsin(|w_2 - w_1|/2R)$.
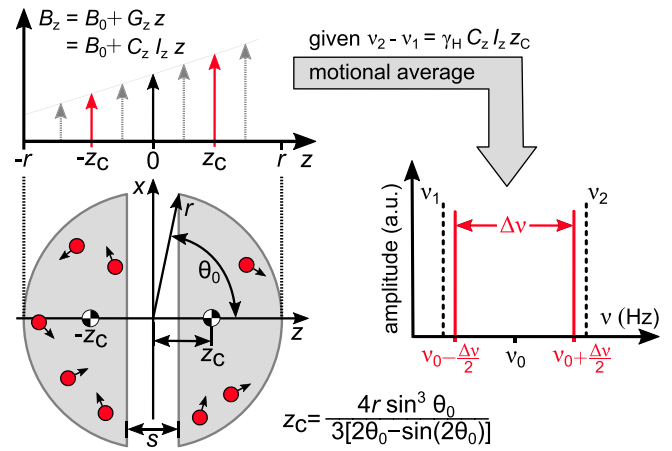

FIG. 3. Cross section of a cylindrical sample cell with two separated compartments in the shape of equal circular segments. Both compartments are exposed to a total magnetic field $B_z = B_0 + zG_z$, where B_0 is a homogeneous magnetic field and G_z the magnetic field gradient. Both compartments are RASER active since they contain sufficiently negative polarized ^{1}H spins ($d_0 > 10^{17}$). Parahydrogen (p-H_2) bubbles (red) move the liquid fast enough such that all ^{1}H spins in each compartment experience an average magnetic field strength given by $B_{av} = B_0 \pm z_c G_z$. The center of gravity z_c is given by Eq. (3). The averaging process produces two ^{1}H Larmor frequencies, ν_2 and ν_1 (black dotted lines on the right) in each compartment. The two red lines on the right correspond to the observed frequencies in the RASER spectrum, which are separated by $\Delta\nu$.

Figure 2(b) shows a plot of the numerically evaluated frequency difference $\Delta\nu$ as a function of the frequency difference $\nu_2 - \nu_1$. At a fixed value for the coupling strength $R = 12.6\,\text{s}^{-1}$, the transition into the synchronized motion (the collapse into one line with $\Delta\nu = 0$) occurs at $|\nu_2 - \nu_1| = R/\pi = 4.01\,\text{s}^{-1}$. Far from this region, i.e., for $|\nu_2 - \nu_1| \gg R$, $\Delta\nu$ is linear in the argument $\nu_2 - \nu_1$, more specifically $|\Delta\nu/(\nu_2 - \nu_1)| = 1$. For values of $\nu_2 - \nu_1$ between the linear and the collapse regime, $\Delta\nu$ vs $\nu_2 - \nu_1$ is a nonlinear function with a corresponding differential slope in absolute units larger than one.

In summary, for the two nonlinear coupled oscillators moving in 1D space, either a frequency comb with an associated nonlinear frequency shift or a synchronized (collapsed) regime is observable. Multiple frequency doubling and chaos could not be observed in the 1D space. This is expected by the Poincaré-Bendixson theorem [44], which predicts the existence of chaos to require at least three dimensions.

B. Gradient-controlled two-compartment RASER model in the (d, A, Ψ) space

We derive here the simplest possible model for a RASER with two independently pumped compartments, which in the presence of a magnetic field gradient G_z oscillate at two average angular frequencies ω_1 and ω_2. The corresponding scheme is shown in Fig. 3. A cross section of a cylindrical sample is shown (bottom left), which is composed of two equal circular

segments with radius r and separated by a slide of thickness s. Both compartments contain a liquid with chemically equivalent RASER active ^{1}H spins, evolving in a magnetic field $B(z) = B_0 + z\, G_z$ (top left). The ^{1}H angular frequency along the central position at $z = 0$ is given by $\omega_0 = \gamma_H B_0$, where the gyromagnetic ratio of the ^{1}H spins is given by $\gamma_H = 2\pi \times 4.257$ Hz/mG. The gradient coil produces a field $z\, G_z = C_z I_z\, z$. Without motion of the liquid, the ^{1}H Larmor frequency would be a linear function of z. We assume that by the pumping mechanism, all voxels of the sample are moving fast enough (a few centimeters per second; see Appendix D) such that the ^{1}H spins of each compartment experience an average magnetic field strength. This average field, indicated by red arrows in the top of Fig. 3, is given by the magnetic field at the two centers of gravity at $\pm z_c$ in each compartment, i.e., by $B(\pm z_c) = B_0 \pm z_c G_z$.

Assuming equal sample geometries and pumping conditions, both compartments experience the same average dipolar field $\langle B_{\text{dip}} \rangle = 6.4$ nT (see Appendix D). The value for $\langle B_{\text{dip}} \rangle$ adds to the static field B_0 and generates only a small offset. Although distant dipolar fields play a significant role in several nonlinear NMR and MRI experiments [18,23,29,30,45,46,50,51] they are insignificant for the phenomena as presented here due to motional averaging. The average angular ^{1}H frequencies ω_μ, $\mu = 1, 2$ in both compartments can be expressed as

$$\omega_\mu = \gamma_H [B_0 + (2\mu - 3) G_z z_c], \quad \mu = 1,\, 2. \quad (2)$$

The center of gravity z_c can be calculated for the known geometry of the sample. Assuming a homogeneous spin density, the number of spins at a slice of thickness dz at position z is $S_d(z) dz$, where the function $S_d(z)$ in Fig. 3 describes a circular arc with a maximum value at angle θ_0 at position $z = s/2$. For $z > 0$ the center of gravity for the right compartment is given by $z_c = (1/N) \int_0^r S_d(z)\, z\, dz$, where $N = \int_0^r S_d(z)\, dz$ is the total number of spins in the right compartment. By symmetry arguments, the center of gravity in the left compartment is $-z_c$. After a coordinate transformation $z = r \cos\theta$ the integral over dz can be rewritten as an integral over $d\theta$, and the center of gravity becomes $z_c = r \int_0^{\theta_0} \sin^2\theta\, \cos\theta\, d\theta / \int_0^{\theta_0} \sin^2\theta\, d\theta$. The maximum angle θ_0, as indicated in the bottom of Fig. 3, is connected to the radius r and thickness s by $\theta_0 = \arccos(s/2r)$. An evaluation of the integrals leads to an analytical expression for the center of gravity

$$z_c = \frac{4r \sin^3 \theta_0}{3[2\theta_0 - \sin(2\theta_0)]}. \quad (3)$$

As a result of the averaging process, the two compartments of the RASER will oscillate at two frequencies $\nu_\mu = \nu_0 + (2\mu - 3)(\gamma_H/2\pi) C_z I_z z_c$, $\mu = 1, 2$, which are indicated by the dashed lines at the bottom right of Fig. 3. According to Eq. (3) and with $s = 1$ mm, $r = 4$ mm ($\theta_0 = 1.4454$) the center of gravity is calculated as $z_c = 0.197$ cm. For magnetic field gradients used in our experiments ranging from -3.84 mG/cm $< G_z < 3.07$ mG/cm the range of frequency separations between the two compartments is given by -6.4 Hz $< \nu_2 - \nu_1 < 5.12$ Hz.

The simplest possible equation of motion for the two-compartment RASER, which can be compared to experiments of two interacting RASER modes with equal amplitudes, is given by

$$\dot{d} = \Gamma(d_0 - d) - \frac{d}{T_1} - 8\beta A^2 (1 + \cos\Psi), \quad (4)$$

$$\dot{A} = \left(\beta d - \frac{1}{T_2^*}\right) A + \beta d A \cos\Psi, \quad (5)$$

$$\dot{\Psi} = \gamma_H 2 z_c G_z - 2\beta d \sin\Psi. \quad (6)$$

In Eqs. (4)–(6), d, A, and Ψ are the population inversion, transverse spin component, and phase difference $\Psi = \phi_2 - \phi_1$. Both modes have equal amplitudes $A_1 = A_2 = A$ and population inversions $d_1 = d_2 = d$ (see Appendix A for the derivation). In the following, the model represented by Eqs. (4)–(6) will be termed the 3D model, since the motion is in the three-dimensional (d, A, Ψ) space. $1/T_2^*$ and $1/T_1$ are the effective transverse and the longitudinal relaxation rates, respectively. d_0 and Γ are the equilibrium population inversion and the pumping rate, which are assumed to be equal for both modes. The coupling constant between the two modes is given by $\beta = \mu_0 \hbar \gamma_H^2 \eta Q/(4V_s)$, where μ_0 is the vacuum permeability, $\hbar$ is Planck's constant, Q is the quality factor of the LC resonator, V_s denotes the sample volume, and $\eta = [0, 1]$ denotes the filling factor of the detection coil.

The parameters used for the simulations were measured or calculated based on the actual experimental conditions. The coupling parameter β is calculated from experimental parameters ($Q = 100$, $V_s = 0.42$ cm^3, $\eta = 0.66$), i.e., $\beta = 3.7 \times 10^{-16}$ s^{-1}. For $T_2^* = 0.4$ s, $T_1 = 6$ s, and $\Gamma = 0.12$ s^{-1}, the RASER threshold is $d_{\text{th}} = 1.6 \times 10^{16}$ (see Appendix A). For each compartment with $V_s/2 = 2.1 \times 10^{-4}$ L the equilibrium population inversion d_0 can be estimated from the ^{1}H polarization $P_H \approx -3 \times 10^{-3}$, the concentration of the pyrazine molecules $c_{\text{pyr}} \approx 0.1$ mol/L, the number of protons $n_{\text{pyr}} = 4$, and $N_A = 6.023 \times 10^{23}$/mol. The estimated value is $d_0 = c_{\text{pyr}}(V_s/2)(-P_H) n_{\text{pyr}} N_A = 1.52 \times 10^{17}$. A minus sign in front of the negative-valued polarization P_H ensures that the condition $d_0 > 0$ for RASER action holds. In a RASER experiment with 100 s duration typical fluctuations of Γ and d_0 are on the order of 10%–20%. For the two compartments, and on the timescale of our measurements ($\sim$30 s), this fluctuation in d_0 corresponds to a dipolar-field-induced frequency difference of about ± 27 mHz, which is superimposed by frequency drifts of $\sim$100 mHz induced by B_0 field fluctuations in the field of the electromagnet.

The 3D model Eqs. (4)–(6) opens the possibility for chaotic motion, since according to the Poincaré-Bendixson theorem the minimum number of dimensions for chaos is three [44]. The chaotic regime might eventually be accompanied by multiple period doubling and by mode collapse. In order to explore experimentally at which frequency differences all these phenomena occur, it is crucial that the mode separation $\omega_2 - \omega_1 = \gamma_H 2 z_c G_z$ can be controlled precisely while the other parameters T_1, T_2^*, d_0, β, and Γ are known and kept constant.
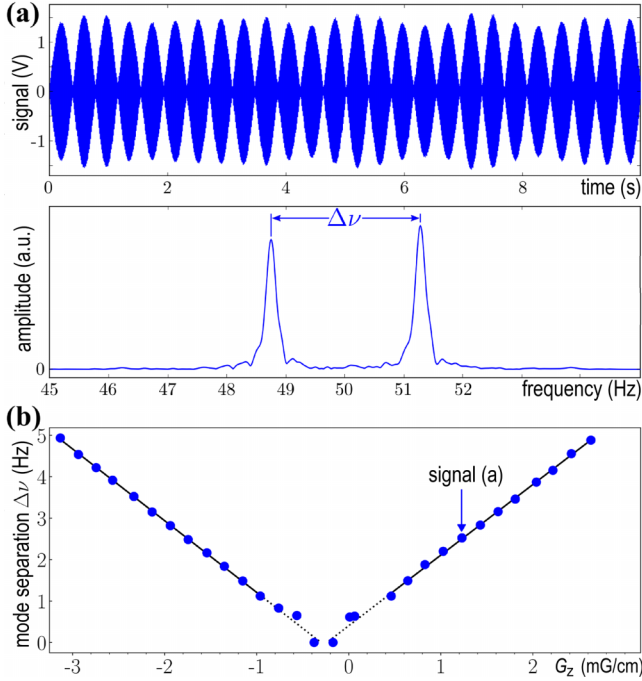
FIG. 4. Measured separation between two RASER modes $\Delta\nu$ vs the gradient G_z. (a) Top: ^{1}H RASER signal of SABRE-pumped pyrazine measured at $B_0 = 7.8$ mT (333.3 kHz ^{1}H Larmor frequency) and for $G_z = 1.152$ mG/cm. Bottom: The corresponding Fourier transformed spectrum shows two lines separated by $\Delta\nu = 2.52$ Hz. The RASER signal has been folded with a Hamming window in order to avoid sinc artifacts. The off-resonance center frequency is $\nu_0 = 50$ Hz. (b) Measured mode separation $\Delta\nu$ (circles) vs gradient G_z. All data points with $|G_z| > 0.77$ mG/cm fit well to two linear functions (solid lines) with a slope given by $|(2\pi)^{-1}\gamma_H 2z_c| = 1.771$ Hz cm/mG.

IV. EXPERIMENTAL RESULTS AND COMPARISON WITH THEORY

Figure 4(a) shows the measured signal from the two-compartment ^{1}H RASER for an applied gradient $G_z = 1.15$ mG/cm and a small residual laboratory gradient. The total gradient (applied and residual gradient) corresponds to a mode separation of $|\nu_2 - \nu_1| = 2.52$ Hz. The beat signal with a minimum amplitude of nearly zero indicates the presence of two equal RASER modes $A_{1,2} = A$. The corresponding spectrum in the absolute mode on the bottom of Fig. 4(a) consists of two lines with similar amplitudes separated by $\Delta\nu = 2.52$ Hz.

The value for the rate R, which corresponds to the two-dimensional RASER model, obtained after adiabatic elimination of the fast-changing variable d (slaving principle) and by assuming $d_0 = 1.2 \times 10^{17}$, results in $R = \beta d_0 \approx 44.4$ s^{-1} (see Appendix B). According to the 1D model, a line collapse is expected for $|\nu_2 - \nu_1| < R/\pi = 14.1$ Hz, and a frequency comb appears for $|\nu_2 - \nu_1| > 14.1$ Hz. Here we note that a collapse for the adiabatically eliminated 2D model occurs at $|\nu_2 - \nu_1| < 3.85$ Hz (see Appendix B). Our measurements reveal that for $|\nu_2 - \nu_1| > 2.5$ Hz (for gradients $|G_z| > 2.04$ mG/cm) neither a collapse nor a frequency comb is observed. This is in stark contrast with the expectations of

both the 1D and the 2D model. For the 3D model given by Eqs. (4)–(6), all nonlinear phenomena occur at the much lower values $|\nu_2 - \nu_1| < 2.5$ Hz, and for $|\nu_2 - \nu_1| > 2.5$ Hz a linear dependence $\Delta\nu = \nu_2 - \nu_1 = (\gamma_H/\pi)2z_c G_z$ is expected. This is experimentally proven by Fig. 4(b), where the measured values for $\Delta\nu$ (blue circles) are plotted versus the applied G_z. An exact proportionality between $\Delta\nu$ and G_z is observed outside the range -1 mG/cm $< G_z < 0.67$ mG/cm. The two slopes with positive and negative sign are determined by linear regressions (solid blue lines), which have the same absolute values $|(\gamma_H/\pi)2z_c| = 1.771$ Hz cm/mG. From this slope, the center of gravity is given as $z_c = 0.208$ cm. This value z_c is slightly higher than the theoretically expected value of $z_c = 0.197$ cm, which follows from Eq. (3) using $\theta_0 = \arccos(s/2r)$ with $r = 4$ mm, $s = 1$ mm. The difference of about 5% between the measured and the theoretical z_c can be explained by the adhesive used to fix the glass slide within the glass cylinder, increasing the average thickness of the slide. The regression functions in Fig. 4(b) intersect the G_z axis at an offset gradient $G_z^{\text{off}} = -0.299$ mG/cm. In summary, as a result from the measurements shown in Fig. 4, the frequency separation is given by $\nu_2 - \nu_1 = 1.771$ Hz cm/mG $(G_z + 0.299$ mG/cm).

We will now discuss the cases of mode separations of $|\nu_2 - \nu_1| < 2$ Hz. Figure 5 shows five different scenarios, which correspond to (a) frequency comb, (b) period doubling (p-2), (c) twofold period doubling (p-4), (d) chaos, and (e) mode collapse (synchrony). On the left side in blue the measured spectra are shown together with the corresponding RASER signals (insets). The signals are measured over a time period ranging from 20 s to 85 s. A symmetrical Hamming window is applied to the signal prior to the Fourier transformation to suppress sinc wiggles. The chosen signal lengths and corresponding Hamming windows are a good compromise between the lowest possible influence of magnetic field fluctuations and sufficient spectral resolution. The five panels on the right (red) are the results from numerical simulations, which are based on the 3D model described by Eqs. (4)–(6). The corresponding initial conditions and the simulation parameters β, Γ, T_1, T_2^*, d_0, and $\nu_2 - \nu_1$ are given in the caption of Fig. 5. The values of these parameters are derived from measurements or from experimental parameters, as described at the end of Sec. III B. As a key result, there is excellent agreement between all five measured and the simulated nonlinear phenomena, given the common set of parameters and the same preset values for $\nu_2 - \nu_1$.

In Fig. 5(a) on the left, at $\nu_2 - \nu_1 = 1.57$ Hz, a first glimpse of a frequency comb is visible, showing two major lines separated by $\Delta\nu = 1.49$ Hz accompanied by two smaller lines separated by the same $\Delta\nu$ from their larger neighbors. Most features of the spectrum and the signal, such as shape, line amplitudes, and separation $\Delta\nu$, agree well with the simulation shown on the right.

In Fig. 5(b) on the left, at $\nu_2 - \nu_1 = 1.26$ Hz the spectrum of the measured frequency comb shows a separation of $\Delta\nu = 1.12$ Hz between two consecutive lines. Additional lines can be identified exactly at half the distance $\Delta\nu/2$ between two consecutive major lines. This is the first sign for a period doubling (p-2) process. The simulated spectrum on the right reflects nearly all the basic features of the measured
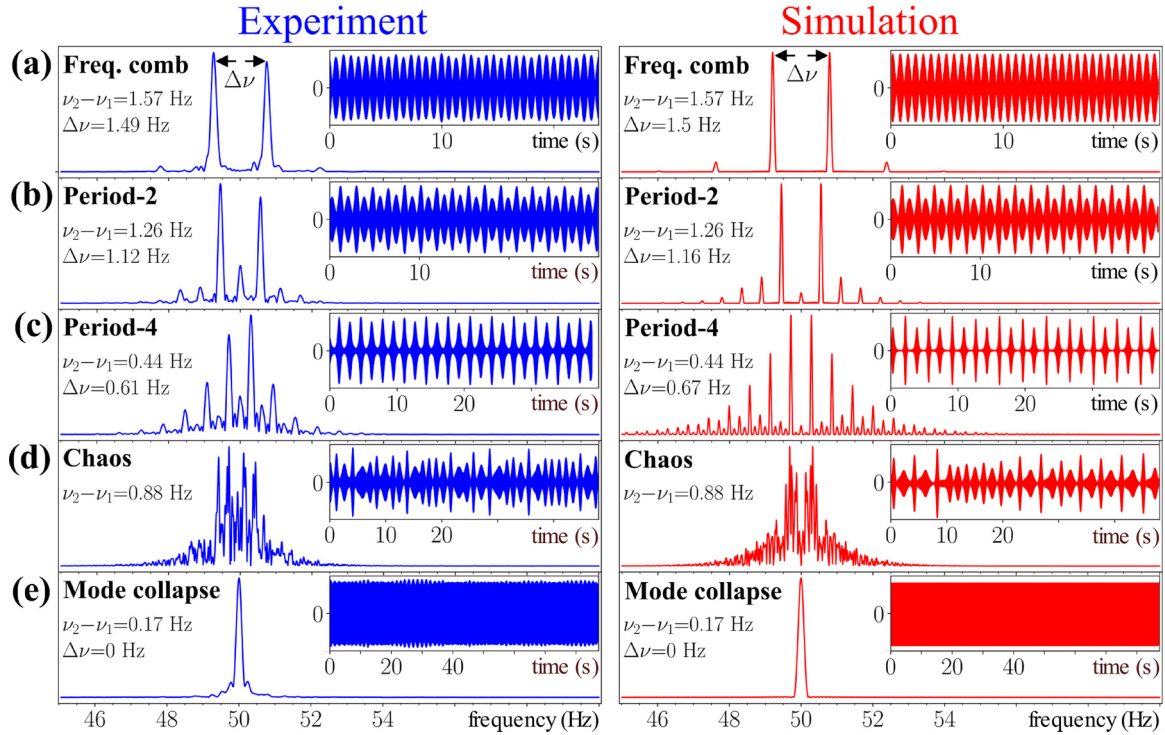
FIG. 5. Comparison between five measured (blue) and simulated (red) nonlinear phenomena which can arise in a two-mode ^{1}H RASER. These five phenomena are (a) frequency comb, (b) period doubling (period-2), (c) twofold period doubling (period-4), (d) chaos, and (e) mode collapse (synchronous motion). All panels show spectra in the absolute mode obtained after Fourier transformation of the corresponding RASER signals shown in the insets. The simulations (a)–(e), which are based on the 3D-theory given by Eqs. (4)–(6), are calculated for five different mode separations $\nu_2 - \nu_1 = \{1.57, 1.26, 0.44, 0.88, 0.17\}$ Hz. The corresponding parameters are $\beta = 3.7 \times 10^{-16}\text{s}^{-1}$, $T_1 = 6$ s, and $T_2^* = \{0.4, 0.39, 0.36, 0.4, 0.4\}$ s, $d_0 = \{1.5, 1.56, 1.6, 1.5, 1.2, 1.23\} \times 10^{17}$, $\Gamma = \{0.12, 0.116, 0.16, 0.12, 0.12\}\text{ s}^{-1}$. Initial conditions: $\phi_1(0) = \phi_2(0) = 0$, $A(0) = 10^{10}$, $d(0) = 0$. The zero time in the insets is not identical to the initial time at $t = 0$. For high resolution, and to prevent sinc artefacts in the simulated spectra, 100 s of the simulated signal duration is folded with a Gauss window. For the measurements, this window is typically 20 to 40 s, which is a good compromise between magnetic field fluctuations and spectral resolution.

spectrum, except for a slightly larger separation $\Delta\nu = 1.16$ Hz and simulated amplitudes of the p-2 lines that differ from the amplitudes in the measured spectrum.

In Fig. 5(c) on the left, at $\nu_2 - \nu_1 = 0.44$ Hz the frequency comb now consists of 10 lines, and the separation is $\Delta\nu = 0.61$ Hz $> |\nu_2 - \nu_1| = 0.44$ Hz. The same is true for the simulated spectrum on the right. This is in stark contrast to the predictions made by the 1D and 2D models, which predict $\Delta\nu < |\nu_2 - \nu_1|$ in the nonlinear regime. Moreover, a twofold period doubling (p-4) is visible in both the measured and simulated spectrum. In each frequency interval $\Delta\nu$ between two consecutive major lines, three smaller lines appear, which divide the interval $\Delta\nu$ into four subintervals of $\Delta\nu/4$.

In Fig. 5(d) on the left, at $\nu_2 - \nu_1 = 0.88$ Hz, the spectrum as well as the RASER signal contains chaotic features. A first hint for chaos is that in the measurement window of 85 s, the RASER signal envelope for a certain interval of several seconds at $t = t_0$ never repeats at a later time $t = t_1$. The second hint for chaos is referring to certain features of the spectrum. Both the experimental and simulated spectrum show a continuum of lines distributed over a frequency interval of about 4 Hz. The envelope of this spectrum roughly decays from the center at $\nu_0 = 50$ Hz in a hyperbolic manner, i.e., proportional to $1/(\nu - \nu_0)$. This decay is consistent with a criterion for chaos shown by Haken [52]. Clear evidence for chaos based

on the exponential divergence of initially close trajectories will be shown at the end of this section. In Fig. 5(e), at $\nu_2 - \nu_1 = 0.17$ Hz, the measured and simulated spectra have collapsed into one line, and the corresponding RASER signals are pure sinusoidal waves. The lines of the two compartments oscillate in synchrony at one common central frequency (here $\nu_0 = 50$ Hz) and with a constant phase shift.

Figure 6 is an overview of the measured and simulated mode separations $\Delta\nu$ vs $\nu_2 - \nu_1$ for the 1D, 2D, and 3D models. Figure 6(a) shows the results of three numerical simulations in order to compare the 1D (green line), 2D (brown line), and 3D model (red line). To ensure a valid comparison, the same rates $R_{1D} = 44.6\text{ s}^{-1}$ and $R_{2D} = \beta d_0 = 44.6\text{ s}^{-1}$ ($d_0 = 1.2 \times 10^{17}$) are assumed for the 1D and 2D model, respectively. Since no pumping rate Γ occurs in the 2D theory (see Appendix B) and no rate R in the 3D theory, the 2D and 3D simulations can be compared only if the same common parameters are chosen (here $T_1 = 6$s, $T_2^* = 0.4$ s, $d_0 = 1.2 \times 10^{17}$, $\beta = 3.7 \times 10^{-16}\text{s}^{-1}$). The blue circles, triangles, and squares in Figs. 6(a) and 6(b) indicate measured values for line separations $\Delta\nu$, $\Delta\nu/2$ (p-2), and $\Delta\nu/4$ (p-4). The shaded area in (a) indicates the region where frequency combs, period n, chaos, and synchrony are experimentally observed. Only the 3D model is in accordance with all of the experimental results. The three points of collapse at $\nu_2 - \nu_1 = \{14, 3.8, 0.23\}$ Hz
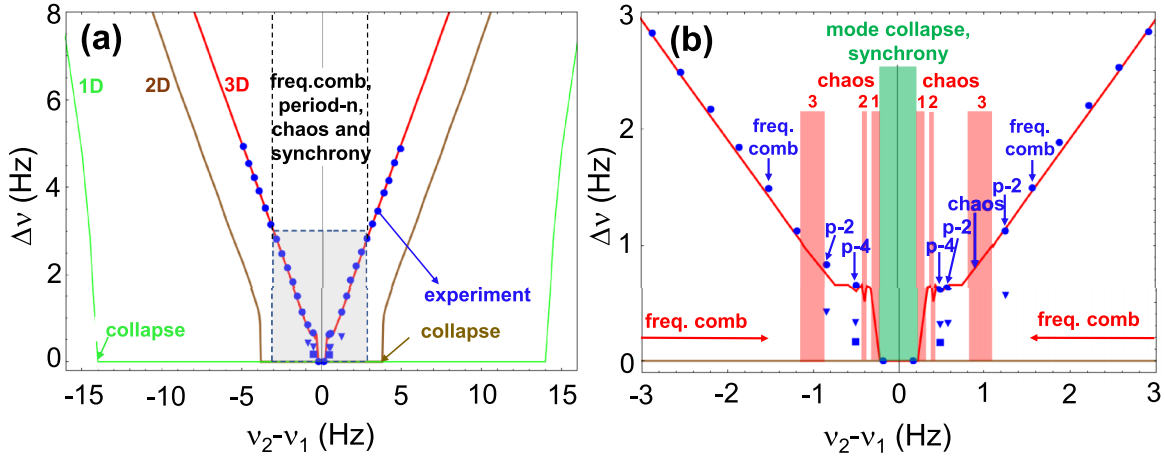
FIG. 6. (a) Comparison between 1D (green), 2D (brown), and 3D model (red) for two nonlinear interacting oscillators (1D), and the two-compartment RASER in two and three dimensions. The simulated frequency separation $\Delta\nu$ is plotted vs the frequency difference $\nu_2 - \nu_1$. Solid circles in (a) and (b) represent measured line separations $\Delta\nu$; triangles and squares symbolize measured separations $\Delta\nu/2$ (period-2) and $\Delta\nu/4$ (period-4), respectively. The gray shaded area in (a) indicates the range where frequency combs, period doublings, chaos, and synchrony (mode collapse) are observed. (b) Expanded view of the gray area in (a), showing more details. Symbols p-2 and p-4 stand for measured period doubling and twofold period doubling, respectively. The three simulated chaotic regimes (1, 2, 3, red areas) are located left and right from the region of synchrony (green area). Simulation parameter for 1D model: $R = 44.6\,\mathrm{s}^{-1}$. 2D model: $T_2^* = 0.4\,\mathrm{s}$, $\Gamma = 100\,\mathrm{s}^{-1} \gg 1/T_2^*$, $d_0 = 1.2 \times 10^{17}$, $\beta = 3.72 \times 10^{-16}\mathrm{s}^{-1}$. 3D model: $T_2^* = 0.4\,\mathrm{s}$, $T_1 = 6\,\mathrm{s}$, $\Gamma = 0.12\,\mathrm{s}^{-1}$, $d_0 = 1.2 \times 10^{17}$, $\beta = 3.72 \times 10^{-16}\mathrm{s}^{-1}$.

for the 1D, 2D, and 3D model are far from each other. A possible explanation is that with increasing number of dimensions, the corresponding two RASER trajectories are less restricted in their configuration space. This reduces their effective interaction, with the consequence that the regime of mode collapse becomes smaller.

The enlarged view in Fig. 6(b) shows the measured and simulated windows for period-*n*, chaos, and synchrony. All measurements (blue circles) associated with frequency combs, period-2, period-4, chaos, and mode collapse are marked by arrows. Three chaotic regimes indicated by 1, 2, and 3 (red areas) left and right from the regime of mode collapse (green area) are predicted by the simulation. The experimentally observed chaos at $\nu_2 - \nu_1 = 0.88\,\mathrm{Hz}$ lies within the simulated region 3 of chaos with $0.83\,\mathrm{Hz} < |\nu_2 - \nu_1| < 1.09\,\mathrm{Hz}$. In the 3D (d, A, Ψ) space, chaos is characterized by a never-closing strange attractor [44]. Close to each chaotic window, the associated trajectory of period-*n* circles *n* times per period in the (A, d) space before closing. Note that both chaotic windows denoted by $1(0.22\,\mathrm{Hz} \leqslant |\nu_2 - \nu_1| < 0.32\,\mathrm{Hz})$ are lying very close to the regime of synchrony given by $|\nu_2 - \nu_1| < 0.22\,\mathrm{Hz}$. We remark that a larger number of additional period-*n* windows ($n = 3, 5, 6, 8, 10$) have been found in simulations, but not experimentally verified (see Appendix C).

Finally, we present a more concise test that the measured and simulated RASER signals in Figs. 5 and 6 indeed represent a chaotic regime. One intrinsic characteristic of chaotic behavior is the extreme sensitivity towards changes in initial conditions. Two trajectories are chaotic when they start extremely close together and very soon diverge in an exponential manner. This is demonstrated in Fig. 7. In each panel two RASER trajectories (red and green lines) are simulated, which differ only by their initial small phase difference $\Psi^{\mathrm{red}}(0) = \phi_2^{\mathrm{red}}(0) - \phi_1^{\mathrm{red}}(0) = 0$ and $\Psi^{\mathrm{gr}}(0) = \phi_2^{\mathrm{gr}}(0) -$

$\phi_1^{\mathrm{gr}}(0) = 10^{-13}$. All other simulation parameters and initial values are equal for both trajectories (see caption). The two RASER trajectories in Figs. 7(a) and 7(b) were chosen as a reference in order to compare with the adjacent chaotic regimes. The first two RASER signals in Fig. 7(a) represent a period-4 trajectory, with $\nu_2 - \nu_1 = 1.107\,\mathrm{Hz}$ located close above the chaotic window $3(0.85\,\mathrm{Hz} < \nu_2 - \nu_1 < 1.09\,\mathrm{Hz})$. Figure 7(b) corresponds to a period-2 trajectory simulated at $\nu_2 - \nu_1 = 0.35\,\mathrm{Hz}$, which is close to the chaotic window $1(0.21\,\mathrm{Hz} < \nu_2 - \nu_1 < 0.32\,\mathrm{Hz})$. If the trajectories in Figs. 7(a) and 7(b) were not chaotic, the signals and the spectra (insets) should be insensitive to a small change in the initial conditions. Indeed, neither the two trajectories (red and green) nor the corresponding two spectra in Figs. 7(a) and 7(b) can be distinguished.

This high sensitivity to small changes in the initial conditions is shown in Fig. 7(c). Two RASER signals with a phase difference of 10^{-13} are simulated at $\nu_2 - \nu_1 = 0.88\,\mathrm{Hz}$, which is inside the chaotic window 3. The two signals are identical for the first 40 s, but for $t > 40\,\mathrm{s}$ they become significantly different. The corresponding two spectra in the inset, which result from a Fourier transformation on the window $60\,\mathrm{s} < t < 260\mathrm{s}$, are broad and very different. The diverging two trajectories can also be observed in Fig. 7(d) with $\nu_2 - \nu_1 = 0.27\,\mathrm{Hz}$, which lies close above the point of collapse (synchrony) at $0.22\,\mathrm{Hz}$. Compared to Fig. 7(c), the two chaotic trajectories start to diverge at a later time $t > 60\,\mathrm{s}$, and the two different chaotic spectra are broader.

V. CONCLUSION AND OUTLOOK

In conclusion, the physics of the two-compartment RASER has been investigated with respect to nonlinear phenomena such as frequency combs, nonlinear frequency shifts,
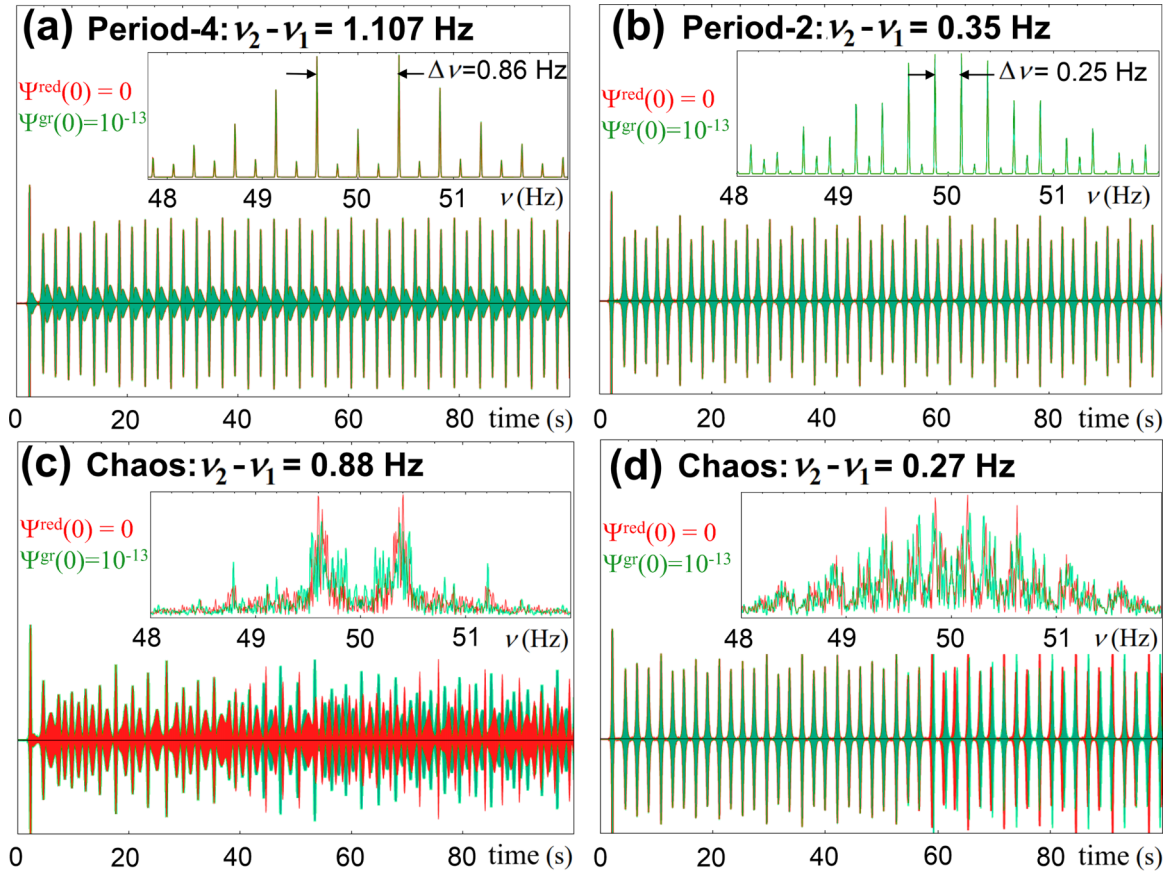
FIG. 7. Proof of chaos using the method of divergence for two RASER trajectories starting initially very close together. (a)–(d) Simulations of two-mode RASER signals at four different values $\nu_2 - \nu_1 = 1.107\,\text{Hz}$ (a), $0.35\,\text{Hz}$ (b), $0.88\,\text{Hz}$ (c), and $0.27\,\text{Hz}$ (d). Corresponding spectra are shown in the insets. The simulation parameters and initial values for two trajectories in red and green are identical: $T_1 = 6\,\text{s}$, $T_2^* = 0.4\,\text{s}$, $d_0 = 1.2 \times 10^{17}$, $\beta = 3.72 \times 10^{-16}\,\text{s}^{-1}$, and $\Gamma = 0.12\,\text{s}^{-1}$, $d(0) = 0$, $A(0) = 10^{10}$. The initial phase difference $\Psi(0) = \phi_2(0) - \phi_1(0)$ between the two trajectories differ by only 10^{-13}: $\Psi^{\text{red}}(0) = \phi_2^{\text{red}}(0) - \phi_1^{\text{red}}(0) = 0$ and $\Psi^{\text{gr}}(0) = \phi_2^{\text{gr}}(0) - \phi_1^{\text{gr}}(0) = 10^{-13}$. In (a), $\nu_2 - \nu_1 = 1.107\,\text{Hz}$, two identical period-4 RASER trajectories are shown. The two corresponding spectra cannot be distinguished. The same is true for the period-2 signals and spectra in (b) with $\nu_2 - \nu_1 = 0.35\,\text{Hz}$. In (c), $\nu_2 - \nu_1 = 0.88\,\text{Hz}$, which is an example for chaos, the two trajectories diverge for $t > 45\,\text{s}$. The two corresponding broad spectra differ significantly. Similar features for chaos are shown in (d), for $\nu_2 - \nu_1 = 0.27\,\text{Hz}$, where the divergence starts at $t > 60\,\text{s}$. All spectra have been transformed using a time window $60\,\text{s} < t < 260\,\text{s}$.

multiple-period doublings, chaos, and synchrony (mode collapse). Only the two-mode RASER theory evolving in the 3D (d, A, Ψ) space is in full agreement with all experimental results. Therefore, the 3D-RASER theory should be able to predict chaos and synchrony in regimes not accessible for current experiments. This includes the physics of $N > 2$ interacting RASER modes at exceedingly high pumping rates and/or close to the maximum possible polarization $P_{\text{H}} = -1$.

One remarkable result is that under appropriate conditions, the range of mode separation for chaos and synchronous motion lie very close together (see Appendix C). Currently, it is not evident what defines the number of chaotic windows at specific parameter values and how many chaotic windows exist for $N > 2$ modes. These questions will be the focus of future investigations.

We believe that the present experimental and theoretical results are important for several reasons. First, for RASER MRI [39], which has been discovered recently, a deeper understanding of the image formation process is necessary. In

RASER MRI, many RASER active slices interact in the presence of a magnetic field gradient, so synchrony and eventually chaos play an important role for understanding image formation.

Second, spectra showing chaos and multiple period doubling were demonstrated at mode separations $\nu_2 - \nu_1$ much smaller than the line width $\Delta\nu_{\text{L}} = 1/(\pi T_2^*) = 0.8\,\text{Hz}$. This might open a new avenue for high-resolution NMR spectroscopy, where chemical shift differences and J-coupling-induced splittings well below the line width $\Delta\nu_{\text{L}}$ can be measured. The prerequisite is a mathematical model, which assigns the measured spectral features (i.e., the location of chaos and period-n signals) to all involved J couplings and chemical shift differences.

Third, calculations based on the EHQE approach [32,48] show that RASERs pumped with p-H_2, by DNP, or by SEOP can be miniaturized to scales smaller than $100\,\mu\text{m}$ with a moderate loss in signal-to-noise ratio. This approach enables the implementation of microfabricated RASER devices, which can be integrated into electronic circuits, for example, as

on-chip local frequency synthesizers or magnetic field and rotational sensors, or as chaos-based true random generators.

APPENDIX A: GENERAL EQUATION OF MOTION OF THE TWO-COMPARTMENT RASER

In the following, the RASER equations for two compartments will be described. According to the multi-mode RASER equations [33,35,39], the equations of motion for $\mu = 1, 2$ modes are given by a set of six nonlinear coupled differential equations for the population inversions d_μ, the transverse spin components A_μ, and the phases ϕ_μ:

$$\dot{d}_\mu = \Gamma_\mu(d_{\mu,0} - d_\mu) - \frac{d_\mu}{T_1} - 4\beta \sum_{\sigma,\tau=1}^{2} A_\sigma A_\tau \cos(\phi_\sigma - \phi_\tau),$$
(A1)

$$\dot{A}_\mu = -\frac{A_\mu}{T_2^*} + \beta d_\mu \sum_{\tau=1}^{2} A_\tau \cos(\phi_\tau - \phi_\mu), \quad (A2)$$

$$\dot{\phi}_\mu = \gamma_H[B_0 + (2\mu - 3)G_z z_c] + \beta \frac{d_\mu}{A_\mu} \sum_{\tau=1}^{2} A_\tau \sin(\phi_\tau - \phi_\mu).$$
(A3)

For simplicity, the six variables $\{d_1, A_1, \phi_1, d_2, A_2, \phi_2\}$ in Eqs. (A1)–(A3) have two common relaxation rates: one is the effective transverse relaxation rate $1/T_2^*$ for $A_{1,2}$, and the other is the longitudinal relaxation rate $1/T_1$ for $d_{1,2}$. The coupling constant between the two modes is given by $\beta = \mu_0 \hbar \gamma_H^2 \eta Q/(4V_s)$, where μ_0 is the vacuum permeability, $\hbar$ is Planck's constant, Q is the quality factor of the LC resonator, and V_s denotes the sample volume. The factor $\eta = [0, 1]$ denotes the filling factor of the detection coil with respect to the sample volume V_s.

The first term on the right side of Eq. (A1) drives the population inversions d_μ into the equilibrium population inversions $d_{\mu,0}$ by the time-dependent pumping rate Γ_μ, the second term describes the loss due to T_1 relaxation, and the third term denotes a nonlinear decay process proportional to the quadratic terms $A_\sigma A_\tau$. Eq. (A2) describes the evolution of A_μ, where the first term on the right side is a decay of A with the rate $1/T_2^*$. The second term for $\mu = \tau$ increases A_μ with the rate βd_μ, while for $\mu \neq \tau$ the term represents a modulation of A_τ with the factor $\cos(\phi_\tau - \phi_\mu)$. Eq. (A3) describes the evolution of the phases ϕ_μ, which evolve with their specific angular frequencies ω_μ given by the first term on the right of Eq. (A3). The second term causes either a phase modulation

by the factor $\sin(\phi_\tau - \phi_\mu)$ or is responsible for a synchronized motion (a mode collapse) of both modes, depending on the value of βd_μ and on $\omega_2 - \omega_1$. The time-dependent pumping rate and the equilibrium population inversion $d_{\mu,0}$ for each mode are assumed to be different. Under these assumptions, the evolution in the six-dimensional space is highly complicated. Therefore, it makes sense to reduce further the complexity described by Eqs. (A1)–(A3) from the six- into the three-dimensional space. This is achieved by assuming for both modes a constant pumping rate $\Gamma_\mu = \Gamma$ and the same value $d_{\mu,0} = d_0$. By introducing the phase difference given by $\Psi = \phi_2 - \phi_1$, a differential equation for Ψ alone is obtained by subtracting the two Eqs. (A3) for $\mu = 1, 2$ from each other. As a result, Eqs. (A1)–(A3) reduce from six- to the three-dimensional (d, A, Ψ) space [see Eqs. (4)–(6)], which serve as the base model of the two-compartment RASER with two equal amplitudes. A threshold population inversion d_{th} from where RASER activity starts can be derived from Eqs. (4) and (5). If $\beta d > 1/T_2^*$, the bracket on the right side of Eq. (5) becomes positive and $dA/dt > 0$, so the RASER signal starts to grow. Equation (4) states that prior to RASER action ($A = 0$), the maximum value of d is decreased by the factor $(\Gamma + T_1^{-1})/\Gamma$. This, together with Eq. (5), leads to the RASER threshold condition given by $d_{\text{th}} = (\Gamma + T_1^{-1})/(\Gamma \beta T_2^*)$. Provided $\Gamma \gg T_1^{-1}$ holds, T_1 relaxation can be neglected, and the threshold condition becomes simply $d_{\text{th}} = 1/(\beta T_2^*)$.

APPENDIX B: COLLAPSE CONDITION FOR 2D RASER AFTER ADIABATIC ELIMINATION

The dynamics of two RASER modes moving in the (A, Ψ) space (2D model) after adiabatic elimination and an analytical expression for the point of collapse is derived from the equations in the three-dimensional (d, A, Ψ) space [Eqs. (4)–(6)]. We briefly recall the derivation of the equations of motion through adiabatic elimination of fast-varying variables [33,35,52]. Starting with Eqs. (4)–(6), which move in the 3D (d, A, Ψ) space, the population inversion d can be eliminated if $\Gamma \gg 1/T_2^*$, $1/T_1$. Then T_1 relaxation in Eq. (4) can be neglected and the fast-changing variable d can be eliminated by setting $dd/dt = 0$. So Eq. (4) becomes

$$d = d_0 - \frac{8\beta}{\Gamma} A^2(1 + \cos\Psi). \quad (B1)$$

The adiabatic elimination of d means that d follows the slowly changing variables A and Ψ [52]. Now d in Eqs. (5) and (6) is replaced by the right side of Eq. (B1). This leads to the 2D model given by

$$\dot{A} = \left[R(1 + \cos\Psi) - \frac{1}{T_2^*}\right]A - 2L(1 + \cos\Psi)^2 A^3, \quad (B2)$$

$$\dot{\Psi} = (\omega_2 - \omega_1) - (2R - 4LA^2)\sin\Psi + 2LA^2 \sin 2\Psi. \quad (B3)$$

The two rates in R and L in Eqs. (B2) and (B3) are given by

$$R = \beta d_0 \quad \text{and} \quad L = \frac{4\beta^2}{\Gamma}. \quad (B4)$$

Since the evolution in Eqs. (B2) and (B3) of the two RASER modes is restricted to the 2D (A, Ψ) space, multiple-period doubling and chaos are impossible. Numerical simulations reveal the occurence of frequency combs,

nonlinear frequency shifts, and synchrony (mode collapse), similar to the 1D model of two coupled oscillators [Eq. (1)]. We are now interested in where the collapse of Eqs. (B2) and (B3) occurs and compare this result with the collapse in the 1D and 3D model.

The condition for collapse for the 1D model is simply proportional to d_{col}, i.e., $(\nu_2 - \nu_1)_{col} = R/\pi = (\beta/\pi)d_{col}$ where $(\nu_2 - \nu_1)_{col}$ is the frequency difference of where the collapse should occur. For the 2D model, the functional dependence between $(\nu_2 - \nu_1)_{col}$ and d_{col} is more complex. At the collapse, two stationary conditions have to be fulfilled in Eqs. (B2) and (B3), i.e., $dA_s/dt = 0$ and $d\Psi_s/dt = 0$. From the first condition $dA_s/dt = 0$ the squared stationary amplitude can be calculated as $A_s^2 = [R(1 + \cos\Psi) - 1/T_2^*]/[2L(1 + \cos\Psi)^2]$. After replacing A_s^2 in Eq. (B3) and setting $d\Psi_s/dt = 0$, a transcendent condition for the stationary phase Ψ_s at a given $(\nu_2 - \nu_1)_{col}$ can be calculated,

$$\frac{\sin\Psi_s}{1 + \cos\Psi_s} = \frac{T_2^*(\omega_2 - \omega_1)_{col}}{2} = \frac{(\nu_2 - \nu_1)_{col}}{\Delta\nu_L}, \quad \text{(B5)}$$

where in Eq. (B5) $\Delta\nu_L = 1(\pi T_2^*)$ is the line width. An elegant expression for d_{col} can now be derived by inserting the known values for A_s^2 and Ψ_s into Eq. (A4). After some algebraic transformations, the result is

$$d_{col} = \frac{1}{\beta T_2^*(1 + \cos\Psi_s)} = \frac{d_{th}}{(1 + \cos\Psi_s)}, \quad \frac{\pi}{2} \leqslant \Psi_s \leqslant \pi. \quad \text{(B6)}$$

In Eq. (B6), $d_{th} = 1/(\beta T_2^*)$ is the threshold population inversion. The pair of Eqs. (B5) and (B6) constitutes two equations which for a given $(\nu_2 - \nu_1)_{col}$ and line width $\Delta\nu_L$ implicitly fix the stationary phase Ψ_s and d_{col}. Note that the range of the stationary phase must be within $\pi/2 \leqslant \Psi_s \leqslant \pi$. For $0 \leqslant \Psi_s < \pi/2$, which is the possible range for the 1D model, Eq. (B6) predicts $d_{col} \leqslant d_{th}$. So for the 2D model the range $0 \leqslant \Psi_s < \pi/2$ can be excluded since there is no RASER activity below the threshold. Close to threshold, i.e., close to $d_{th} = 1/(\beta T_2^*)$, the stationary value for the phase difference is $\Psi_s = \pi/2$, $(\nu_2 - \nu_1)_{col} = \Delta\nu_L$ and $d_{col} = d_{th}$. Equation (B5) states that for any given frequency difference $(\nu_2 - \nu_1)_{col} > \Delta\nu_L$ there always exists a corresponding stationary phase Ψ_s, and the population inversion for collapse d_{col} is a monotonically increasing function of $(\nu_2 - \nu_1)_{col}$. Finally, for the 3D model we have not found an analytical expression for the point of collapse. Therefore, we have to rely on numerical simulations.

APPENDIX C: DESCRIPTION OF PERIOD DOUBLING AND CHAOTIC REGIMES IN FIG. 6

In this section we present details for all regimes where chaos and multiple-period doubling occur. The simulations are based on Eqs. (4)–(6) and on the set of parameters given in Fig. 6. Due to the symmetry of the simulated spectra with respect to the $(\nu_2 - \nu_1)$ axis, it is sufficient to evaluate only the positive frequency range, i.e., $0 \leqslant \nu_2 - \nu_1 < 3$ Hz. Starting at $\nu_2 - \nu_1 = 0$, the different frequency intervals in units (Hz) for the case of chaos and period-n doubling are listed in square brackets in ascending order. Before each square bracket the following shorthand is introduced: "sy" for synchrony, "ci"

for chaos at window number $i = 1, 2, 3$, and p-n for a period-n process $(n = 1, 2, 3 \ldots)$. p-1 represents a frequency comb. The total sequence S reads

S = {sy[0, 0.23], c1[0.23,0.32], p-6[0.325], p-3[0.33], p-4[0.345], p-2[0.35], p-1[0.26,0.38], c2[0.385,0.39], p-6[0.394], p-4[0.395], p-2[0.4,0.46], p-1[0.48,59], p-2[0.6,0.78], p-4[0.79], p-8[0.8,0.809], p-n[0.81,0.819], c3[0.82,1.09], p-10[1.101], p-5[1.102,1.105], p-4[1.107, 1.109], p-2[1.11, 1.17], p-1[1.18,2]}.

As already shown in Fig. 6, the sequence starts as sy[0,0.23], followed by c1[0.23,0.32]. The chaotic regime c1 is followed by a period-doubling sequence p-6[0.325], p-3[0.33], p-4[0.345] and p-2[0.35], where the number [X] in the brackets stands for a very narrow frequency interval around X. Next comes a frequency comb p-1[0.36,0.38], followed by a second narrow chaotic window c2[0.385,0.39], then a narrow period-n doubling sequence p-6[0.394], p-4[0.395], p-2[0.4,0.46]. It follows a frequency comb p-1[0.48,0.59], and a period-doubling sequence p-2[0.6,0.78], p-4[0.79], p-8[0.8,0.809], p-i[0.81,0.819] $(i > 16)$. Then the third chaotic regime c3[0.82,1.09] is followed by a period-n sequence p-10[1.101], p-5[1.102,1.105], p-4[1.107, 1.109], and p-2[1.11, 1.17]. Finally, at $\nu_2 - \nu_1 = 1.18$ Hz a frequency comb p-1[1.18,2] is observed and is observable in the spectrum up to $\nu_2 - \nu_1 = 3$ Hz. For $\nu_2 - \nu_1 > 2$ Hz, the distance $\Delta\nu$ increases linearly with $\nu_2 - \nu_1$. Note the chaotic region c3 is flanked by two period-n sequences, which is a typical precursor for the onset of chaos. This is not the case for the chaotic regions c1 and c2, which have a period-n process only on one side. Specifically, the left border of the c1 window is adjacent to the region of synchrony.

Another remarkable fact is that the numbers $n = 1, 2, 3, 4, 5, 6, \ldots$ for period-n processes are observed, which occur similarly to the famous universal U sequence given by $U = 1, 2, 2 \times 2, 6, 5, 3, 2 \times 3, 5, 6 \ldots$ as first discovered by Metropolis and Feigenbaum [53,54]. Our results do not exactly reflect the order of the U sequence. One possible reason is that the parameter $\nu_2 - \nu_1$ is not in one-to-one correspondence with the scaling factor α used in the bifurcation map for the 1D logistic equation [44]. Another possible explanation is that the U sequence is valid only for weak chaos, where the corresponding strange attractor has a fractal dimension close above two. Examples for weak chaos are the Lorentz and Rössler attractors [55,56]. If in our case chaos is not weak, and the condition for the U sequence is not fulfilled. Further detailed investigations are necessary to explain all these findings

APPENDIX D: CAVITY PULLING AND DISTANT DIPOLAR FIELDS

In the following, we estimate the effects of cavity pulling and distant dipolar fields (DDFs) for our experimental conditions. We conclude that cavity pulling is negligible and the longitudinal and transversal DDFs are about 100-fold smaller than the radiation damping field.

To estimate the cavity pulling, we consider the case that the line width $\Delta\nu_L$ of the atoms or the spins is much smaller than the frequency width $\Delta\nu_c$ of the cavity or the LC resonator: If $\Delta\nu_L \ll \Delta\nu_c = \nu_c/Q$ holds, the observed RASER frequency

at frequency ν_μ^* deviates from the free ^{1}H RASER frequency ν_μ by [57,58]

$$\nu_\mu^* - \nu_\mu = (\nu_c - \nu_\mu)\frac{\Delta\nu_L}{\Delta\nu_c}. \qquad \text{(D1)}$$

For our two-compartment RASER the ^{1}H line width for $T_2^* = 0.4\,\text{s}$ is $\Delta\nu_L = 1/(\pi T_2^*) = 0.8\,\text{Hz}$, and the two modes oscillate at frequencies $\nu_\mu = (2\pi)^{-1}\gamma_H[B_0 + (2\mu - 3)G_z z_c]$, $\mu = 1, 2$. Given the quality factor $Q = 100$ of the LC resonator resonating at $\nu_c = 333\,\text{KHz}$, so $\Delta\nu_c = 3.33\,\text{kHz}$ and a typical resonance offset $(\nu_c - \nu_\mu) \sim 50\,\text{Hz}$, Eq. (D1) predicts for two modes lying close together (a few Hz) a frequency shift towards ν_c of $(\nu_\mu - \nu_\mu^*) \sim 12\,\text{mHz}$. Specifically for two RASER modes differing by $\nu_2 - \nu_1 = 1\,\text{Hz}$ the relative frequency shift due to cavity pulling is 0.24 mHz, which is much smaller compared to our observed frequency shifts and line splittings (at least a few tens of mHz). Therefore cavity pulling effects can be neglected in all our experiments.

Distant dipolar fields (DDFs) and their nonlinear effects play a significant role in highly polarized nuclear spin ensembles with high spin densities. One recent example is the DNP-pumped solid state ^{1}H RASER [51], where strong DDF effects (chirped RASER pulses) and frequency shifts in the kHz regime have been observed at low temperatures ($T \sim 1.2\,\text{K}$). The number of polarized ^{1}H spins in this experiment were about $d_0 > 5 \times 10^{21}$ for a sample volume $V_s \sim 0.8\,\text{cm}^3$. In a solid the ^{1}H spins are not moving on the timescale of the RASER experiments so DDF effects do substantially contribute to the spin evolution in addition to radiation damping effects. A review of nonlinear NMR spectroscopy in liquids including DDF and radiation damping effects has been published by Desvaux [50].

In our model for two coupled RASER modes [Eqs. (4)–(6)], the radiation damping field $\beta \cdot d(t)$ is about $18\,\text{s}^{-1}$, which is nearly 100-fold larger than the DDFs (0.27 Hz, see below). For each experiment the ratio between radiation damping and DDF effects can be evaluated by inspection of the corresponding time constants τ_{rd} and τ_d, respectively. The radiation damping rate is given by $1/\tau_{rd} = (\mu_0/2)\gamma_H \eta Q M_0$, with positive or negative values for $1/\tau_{rd}$ depending on the sign of the ^{1}H magnetization $M_0 = (\hbar/2)\gamma_H n_s P_H$ (n_s is the ^{1}H number density and P_H the polarization). We define the rate of evolution due to an average DDF field as $1/\tau_d = |\langle\delta\omega_d\rangle| = |\mu_0 \xi \gamma_H M_0|$. In both expressions for $1/\tau_{rd}$ and $1/\tau_d$ the vacuum permeability μ_0, the ^{1}H gyromagnetic ratio γ_H and magnetization M_0 are common. For radiation damping the product between the filling- and the quality factor ηQ is important, while for DDFs the shape factor ξ of the sample matters. This shape factor ranges from $-1/2 \leqslant \xi \leqslant 1$ and is a function of the sample geometry with $\xi = 0$ representing a sphere, $\xi = -1/2$ a long cylinder, and $\xi = 1$ a thin disk. The absolute of the ratio R between the two time constants τ_{rd} and τ_d can now be defined as a function only depending on ξ, η, and Q:

$$R = \left|\frac{\tau_{rd}}{\tau_d}\right| = \frac{2|\xi|}{\eta Q}. \qquad \text{(D2)}$$

For $R = 0$ ($\xi = 0$, spherical sample) any DDF effects are absent, for $R \ll 1$ radiation damping dominates the

spin evolution, and for $R \gg 1$ DDFs dominate the spin evolution. An extreme example for DDF effects in the 10 mHz regime including slow diffusional motion in the gas phase is reported in [59], where the chemical shift of hyperpolarized ^{129}Xe in liquid toluene was measured in the Earth magnetic field. At higher polarization the Xe line of the resting liquid phase shows a substantial line distortion, broadening, and frequency shift with respect to the Xe gas line. Since the experimental conditions in [59] were $Q \sim 10$, $\eta = 0.04$ (2 cm^3 sample volume, 50 cm^3 coil volume), and $|\xi| \sim 0.8$ (slanted cylinder), we get $R = 4$, so DDFs dominate over radiation damping effects. Therefore distant dipolar fields inside the liquid compartment distort and broaden the line shape. However, the shape of the Xe gas line is identical to the Xe gas peak at much lower Xe polarization (with small DDF and radiation damping effects), so apart from a very small average dipolar shift there is no line distortion, although the Xe atoms in the gas phase experience different DDF fields from the liquid phase at different locations in the sample. This is explained by the Xe gas diffusion (coefficient $D_{Xe} \sim 0.1$–$0.2\,\text{cm}^2/\text{s}$ at 1 bar and RT), which average out the local distant dipolar fields' interaction on the timescale of the measurement (tens of seconds). In the resting liquid phase this is not the case since D_{Xe} in liquid toluene is about four orders of magnitude smaller compared to the gas phase, so there is no averaging out of DDF inhomogeneities.

In contrast to the above case in the present two-mode RASER experiments the parameters $Q = 100$, $\eta = 0.66$, and $\xi = -1/2$ (approximately a long half cylinder for each compartment) lead to $R = 0.015 \ll 1$, and radiation damping dominates the spin. Furthermore, the p-H$_2$ bubbles lead to a rather intense convective and turbulent motion of all volume elements in both compartments. The average velocity of these bubbles was estimated to be several cm/s, so the fast random motion corresponds to a diffusion coefficient $D \gg 1\,\text{cm}^2/\text{s}$. Consequently, if the RASER is in a stationary state, all DDF inhomogeneities which lead to a line broadening or to a complex magnetization evolution average out and only an average dipolar field $\langle B_{dip}\rangle$ given by

$$\langle B_{dip}\rangle = \xi\mu_0\left(\frac{\hbar}{2}\right)\gamma_H n_s P_H \qquad \text{(D3)}$$

remains. Given $\xi = -1/2$, $n_s = 2.4 \times 10^{26}/\text{m}^3$ for a pyrazine concentration of $c_{pyr} = 0.1\,\text{mol/L}$ and a ^{1}H polarization $P_H \sim -3 \times 10^{-3}$ the average dipolar field in each compartment is $\langle B_{dip}\rangle \sim 6.3\,\text{nT}$. This corresponds to an average frequency shift of $(\gamma_H/2\pi)\langle B_{dip}\rangle = 0.27\,\text{Hz}$. This shift is in agreement with the measurement of initial relaxation oscillations of the pyrazine two-compartment RASER (at $G_z = 0$). The measured frequency difference between the oscillations before and after the first maximum of the initial RASER signal (where magnetization M_z changes sign) was measured to be between 0.2 Hz and 0.4 Hz depending on the pumping conditions.

Since both compartments have nearly the same shape, volume V_s, polarization P_H, and spin density n_s, both corresponding RASER frequencies are shifted by the same amount of 0.27 Hz, so averaged distant dipolar fields can be neglected

to first order. Only fluctuations of the bubbling and pumping rates between the two compartments, which are on the order of 10%, could be responsible to dipolar differential shift effects in the order of ± 27 mHz. This small shift could be relevant if the frequency difference between the two modes is at the boundary between mode collapse and chaotic window 1 ($\nu_2 - \nu_1 = 0.21$ Hz; see Fig. 6). In this case the RASER signal could change randomly from a collapsed state (one single oscillation) to a chaotic signal.

In conclusion, in the experimentally observed time windows neither cavity pulling nor DDF effects have an appreciable influence on the evolution of the two ^{1}H RASER modes. All measured different scenarios shown in Fig. 6, the chaotic windows, the mode collapse, and multiple period doublings, can be solely explained by the coupling of the two modes by radiation damping, and thus the transitions between these different scenarios can be predicted by the model given by Eqs. (4)–(6).

[1] A. W. Overhauser, Polarization of nuclei in metals, Phy. Rev. **92**, 411 (1953).

[2] T. R. Carver and C. P. Slichter, Experimental verification of the Overhauser nuclear polarization effect, Phys. Rev. **102**, 975 (1956).

[3] C. Griesinger, M. Bennati, H. M. Vieth, C. Luchinat, G. Parigi, P. Höfer, F. Engelke, S. J. Glaser, V. Denysenkov, and T. F. Prisner, Dynamic nuclear polarization at high magnetic fields in liquids, Prog. Nucl. Magn. Reson. Spectrosc. **64**, 4 (2012).

[4] A. J. Pell, G. Pintacuda, and C. P. Grey, Paramagnetic NMR in solution and the solid state, Prog. Nucl. Magn. Reson. Spectrosc. **111**, 1 (2019).

[5] M. A. Bouchiat, T. R. Carver, and C. M. Varnum, Nuclear Polarization in He$_3$ Gas Induced by Optical Pumping and Dipolar Exchange, Phys. Rev. Lett. **5**, 373 (1960).

[6] W. Happer, Optical pumping, Rev. Mod. Phys. **44**, 169 (1972).

[7] S. Appelt, A. B.-A. Baranga, C. J. Erickson, M. V. Romalis, A. R. Young, and W. Happer, Theory of spin-exchange optical pumping of ^{3}He and ^{129}Xe, Phys. Rev. A **58**, 1412 (1998).

[8] Y.-Y. Jau, T. Walker, and W. Happer, *Optically Pumped Atoms* (John Wiley & Sons, Weinheim, 2010).

[9] M. Batz, P.-J. Nacher, and G. Tastevin, Fundamentals of metastability exchange optical pumping in helium, J. Phys.: Conf. Ser. **294**, 012002 (2011).

[10] C. R. Bowers and D. P. Weitekamp, Transformation of Symmetrization Order to Nuclear-Spin Magnetization by Chemical Reaction and Nuclear Magnetic Resonance, Phys. Rev. Lett. **57**, 2645 (1986).

[11] T. C. Eisenschmid, R. U. Kirss, P. P. Deutsch, S. I. Hommeltoft, R. Eisenberg, J. Bargon, R. G. Lawler, and A. L. Balch, Para hydrogen induced polarization in hydrogenation reactions, J. Am. Chem. Soc. **109**, 8089 (1987).

[12] C. R. Bowers and D. P. Weitekamp, Parahydrogen and synthesis allow dramatically enhanced nuclear alignment, J. Am. Chem. Soc. **109**, 5541 (1987).

[13] J. Natterer and J. Bargon, Parahydrogen induced polarization, Prog. Nucl. Magn. Reson. Spectrosc. **31**, 293 (1997).

[14] S. B. Duckett and C. J. Sleigh, Applications of the parahydrogen phenomenon: A chemical perspective, Prog. Nucl. Magn. Reson. Spectrosc. **34**, 71 (1999).

[15] R. W. Adams, J. A. Aguilar, K. D. Atkinson, M. J. Cowley, P. I. P. Elliott, S. B. Duckett, G. G. R. Green, I. G. Khazal, J. López-Serrano, and D. C. Williamson, Reversible interactions with para-hydrogen enhance NMR sensitivity by polarization transfer, Science **323**, 1708 (2009).

[16] R. W. Adams, S. B. Duckett, R. A. Green, D. C. Williamson, and G. G. R. Green, A theoretical basis for spontaneous polarization transfer in non-hydrogenative parahydrogen-induced polarization, J. Chem. Phys. **131**, 194505 (2009).

[17] R. A. Green, R. W. Adams, S. B. Duckett, R. E. Mewis, D. C. Williamson, and G. G. R. Green, The Theory and practice of hyperpolarization in magnetic resonance using parahydrogen, Prog. Nucl. Magn. Reson. Spectrosc. **67**, 1 (2012).

[18] T. Theis, M. L. Truong, A. M. Coffey, R. V. Shchepin, K. W. Waddell, F. Shi, B. M. Goodson, W. S. Warren, and E. Y. Chekmenev, Microtesla SABRE enables 10% nitrogen-15 nuclear spin polarization, J. Am. Chem. Soc. **137**, 1404 (2015).

[19] K. V. Kovtunov, E. V. Pokochueva, O. G. Salnikov, S. F. Cousin, D. Kurzbach, B. Vuichoud, S. Jannin, E. Y. Chekmenev, B. M. Goodson, D. A. Barskiy *et al.*, Hyperpolarized NMR spectroscopy: *d*-DNP, PHIP, and SABRE techniques, Chem.-Asian J. **13**, 1857 (2018).

[20] M. G. Richards, B. P. Cowan, M. F. Secca, and K. MacHin, The ^{3}He nuclear Zeeman maser, J. Phys. B At. Mol. Opt. Phys. **21**, 665 (1988).

[21] T. E. Chupp, R. J. Hoare, R. L. Walsworth, and B. Wu, Spin-Exchange-Pumped ^{3}He and ^{129}Xe Zeeman Masers, Phys. Rev. Lett. **72**, 2363 (1994).

[22] H. Gilles, Y. Monfort, and J. Hamel, ^{3}He maser for earth magnetic field measurement, Rev. Sci. Instrum. **74**, 4515 (2003).

[23] D. J.-Y. Marion, G. Huber, P. Berthault, and H. Desvaux, Observation of noise-triggered chaotic emissions in an NMR-maser, ChemPhysChem **9**, 1395 (2008).

[24] A. G. Zhuravlev, V. L. Berdinskii, and A. L. Buchachenko, Generation of high-frequency current by the products of a photochemical reaction, ZhETF **28**, 150 (1978).

[25] H.-Y. Chen, Y. Lee, S. Bowen, and C. Hilty, spontaneous Emission of NMR signals in hyperpolarized proton spin systems, J. Magn. Reson. **208**, 204 (2011).

[26] A. N. Pravdivtsev, F. D. Sönnichsen, and J.-B. Hövener, Continuous radio amplification by stimulated emission of radiation using parahydrogen induced polarization (PHIP-RASER) at 14 tesla, Chem. Phys. Chem. **21**, 667 (2020).

[27] P. Bösiger, E. Brun, and D. Meier, Solid-State Nuclear Spin-Flip Maser Pumped by Dynamic Nuclear Polarization, Phys. Rev. Lett. **38**, 602 (1977).

[28] D. Abergel, A. Louis-Joseph, and J.-Y. Lallemand, Self-sustained maser oscillations of a large magnetization driven by a radiation damping-based electronic feedback, J. Chem. Phys. **116**, 7073 (2002).

[29] E. M. M. Weber, D. Kurzbach, and D. Abergel, A DNP-hyperpolarized solid-state water NMR MASER: Observation

and qualitative analysis, Phys. Chem. Chem. Phys. **21**, 21278 (2019).

[30] M. A. Hope, S. Björgvinsdóttir, C. P. Grey, and L. Emsley, A magic angle spinning activated ^{17}O DNP raser, J. Phys. Chem. Lett. **12**, 345 (2021).

[31] P. M. TomHon, S. Han, S. Lehmkuhl, S. Appelt, E. Y. Chekmenev, M. Abolhasani, and T. Theis, A versatile compact parahydrogen membrane reactor, Chem. Phys. Chem. **22**, 2526 (2021).

[32] M. Suefke, S. Lehmkuhl, A. Liebisch, B. Blümich, and S. Appelt, Para-hydrogen raser delivers sub-millihertz resolution in nuclear magnetic resonance, Nat. Phys. **13**, 568 (2017).

[33] S. Appelt, A. Kentner, S. Lehmkuhl, and B. Blümich, From LASER physics to the para-hydrogen pumped RASER, Prog. Nucl. Magn. Reson. Spectrosc. **114-115**, 1 (2019).

[34] B. Joalland, N. M. Ariyasingha, S. Lehmkuhl, T. Theis, S. Appelt, and E. Y. Chekmenev, Parahydrogen-induced radio amplification by stimulated emission of radiation, Angew. Chem. Int. Ed. **59**, 8654 (2020).

[35] S. Appelt, S. Lehmkuhl, S. Fleischer, B. Joalland, N. M. Ariyasingha, E. Y. Chekmenev, and T. Theis, SABRE and PHIP pumped RASER and the route to chaos, J. Magn. Reson. **322**, 106815 (2021).

[36] B. Joalland, T. Theis, S. Appelt, and E. Y. Chekmenev, Background-free proton NMR spectroscopy with radiofrequency amplification by stimulated emission radiation, Angew. Chem. Int. Ed. **60**, 26298 (2021).

[37] S. Korchak, L. Kaltschnee, R. Dervisoglu, L. Andreas, C. Griesinger, and S. Glöggler, Spontaneous enhancement of magnetic resonance signals using a RASER, Angew. Chem. **133**, 21152 (2021).

[38] O. G. Salnikov, I. A. Trofimov, A. N. Pravdivtsev, K. Them, J.-B. Hövener, E. Y. Chekmenev, and I. V. Koptyug, Through-space multinuclear magnetic resonance signal enhancement induced by parahydrogen and radiofrequency amplification by stimulated emission of radiation, Anal. Chem. **94**, 15010 (2022).

[39] S. Lehmkuhl, S. Fleischer, L. Lohmann, M. S. Rosen, E. Y. Chekmenev, A. Adams, T. Theis, and S. Appelt, RASER MRI: Magnetic resonance images formed spontaneously exploiting cooperative nonlinear interaction, Sci. Adv. **8**, eabp8483 (2022).

[40] S. H. Strogatz, From kuramoto to crawford: exploring the onset of synchronization in populations of coupled oscillators, Physica D **143**, 1 (2000).

[41] Y. Kuramoto and D. Battogtokh, Coexistence of coherence and incoherence in nonlocally coupled phase oscillators, Nonlinear Phen. Complex Syst. **5**, 380 (2002).

[42] Y. Kuramoto, *Chemical Oscillations, Waves, and Turbulence* (Springer Verlag, Berlin, 2003).

[43] S. Strogatz, *Sync: The Emerging Science of Spontaneous Order* (Penguin, London, UK, 2004).

[44] S. H. Strogatz, *Nonlinear Dynamics and Chaos: With Applications to Physics, Biology, Chemistry, and Engineering* (Avalon Publishing, Boca Raton, 2014).

[45] D. Meier, R. Holzner, B. Derighetti, and E. Brun, Bistability and chaos in NMR systems, in *Evolution of Order and Chaos*, edited by H. Haken (Springer, Berlin, 1982), pp. 146–156.

[46] Y.-Y. Lin, N. Lisitza, S. Ahn, and W. S. Warren, Resurrection of crushed magnetization and chaotic dynamics in solution NMR spectroscopy, Science **290**, 118 (2000).

[47] L. Borkowski and A. Stefanski, FFT bifurcation analysis of routes to chaos via quasiperiodic solutions, Math. Probl. Eng. **2015**, 367036 (2015).

[48] M. Suefke, A. Liebisch, B. Blümich, and S. Appelt, External high-quality-factor resonator tunes up nuclear magnetic resonance, Nat. Phys. **11**, 767 (2015).

[49] M. J. Cowley, R. W. Adams, K. D. Atkinson, M. C. R. Cockett, S. B. Duckett, G. G. R. Green, J. A. B. Lohman, R. Kerssebaum, D. Kilgour, and R. E. Mewis, Iridium N-heterocyclic carbene complexes as efficient catalysts for magnetization transfer from *para*-hydrogen, J. Am. Chem. Soc. **133**, 6134 (2011).

[50] H. Desvaux, Non-linear liquid-state NMR, Prog. Nucl. Magn. Reson. Spectrosc. **70**, 50 (2013).

[51] V. F. T. J. Chacko and D. Abergel, Dipolar field effects in a solid-state NMR maser pumped by dynamic nuclear polarization, Phys. Chem. Chem. Phys. **25**, 10392 (2023).

[52] H. Haken, *Synergetics: An Introduction*, 3rd ed. (Springer, Berlin, 1983).

[53] N. Metropolis, M. L. Stein, and P. R. Stein, On finite limit sets for transformations on the unit interval, J. Combin. Theory A **15**, 25 (1973).

[54] M. J. Feigenbaum, Universal behavior in nonlinear systems, Physica D **7**, 16 (1983).

[55] E. N. Lorenz, Deterministic nonperiodic flow, J. Atmospheric Sci. **20**, 130 (1963).

[56] O. E. Rössler, An equation for continuous chaos, Phys. Lett. A **57**, 397 (1976).

[57] C. H. Townes, 1964 Nobel lecture: Production of coherent radiation by atoms and molecules, IEEE Spectr. **2**, 30 (1965).

[58] A. Winnacker, *Physik von Maser und Laser* (Bibliographisches Institut, Mannheim, 1984).

[59] S. Appelt, F. W. Häsing, H. Kühn, J. Perlo, and B. Blümich, Mobile High Resolution Xenon Nuclear Magnetic Resonance Spectroscopy in the Earth's Magnetic Field, Phys. Rev. Lett. **94**, 197602 (2005).